

GSA Data Repository 2017316

Effects of secondary phases on crystallographic preferred orientations in mylonites

Andrew J. Cross

Department of Earth & Planetary Sciences, Washington University in St. Louis, 1 Brookings Drive, St. Louis, MO 63130

Greg Hirth

Department of Geological Sciences, Brown University, 324 Brook Street, Providence, RI 02912

David J. Prior

Department of Geology, University of Otago, 360 Leith Street, Dunedin 9056, New Zealand

Table DR1: Experimental conditions and results

Run no.	Piston type	Experiment duration (hours)	Finite shear strain, γ^*	Max. sample thickness (mm)	Thinning factor [†]	Peak stress (MPa)	Stress at $\gamma = 1$ (MPa) [§]
<u>Quartz</u>							
W1915	Planar			Hydrostatic hot press			
W1873	Planar	30	1.4	1.3	N/A	747	280
W1903	Tabular	55	2.8	1.4	2.0	583	300
W1905	Cylindrical	53	2.6	1.4	1.9	375	255
<u>Quartz-albite</u>							
W1915	Planar			Hydrostatic hot press			
W1909	Planar	31	1.0	1.4	2.0	298	~150
W1914	Tabular	40	1.4	1.6	2.0	443	~110
W1917	Cylindrical	52	2.7	1.1	2.0	150	134
W1919	Cylindrical	45	2.6	1.1	2.1	161	143
W1921	Tabular	56	2.7	1.3	2.0	690	188
W1924	Tabular	49	1.8	1.4	2.0	553	91

* Measured at the thickest part of each sample (i.e., either side of the piston asperity)

[†] Maximum thickness of sample/ minimum thickness of sample

[§] Stresses marked with “~” are taken from the last point before strengthening due to friction effects

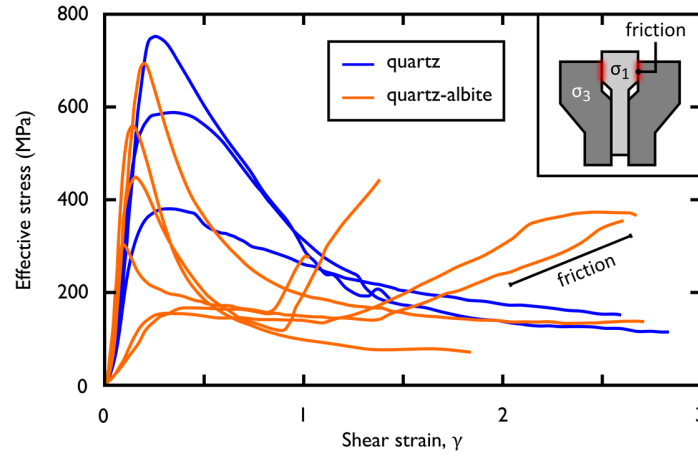


Fig. DR1: Mechanical data from our 9 deformation experiments. Shear strains are those measured in the thickest part of the sample (i.e., either side of the piston asperity). Effective stress is derived from raw force data, corrected for the compliance of the apparatus, but not for changes in the load-supporting area. In some experiments, stress increased beyond a shear strain of ~ 1 due to friction between the σ_1 and σ_3 pistons. This did not impede the advancement of the σ_1 piston, since measured finite shear strains were consistent with the finite σ_1 displacement.

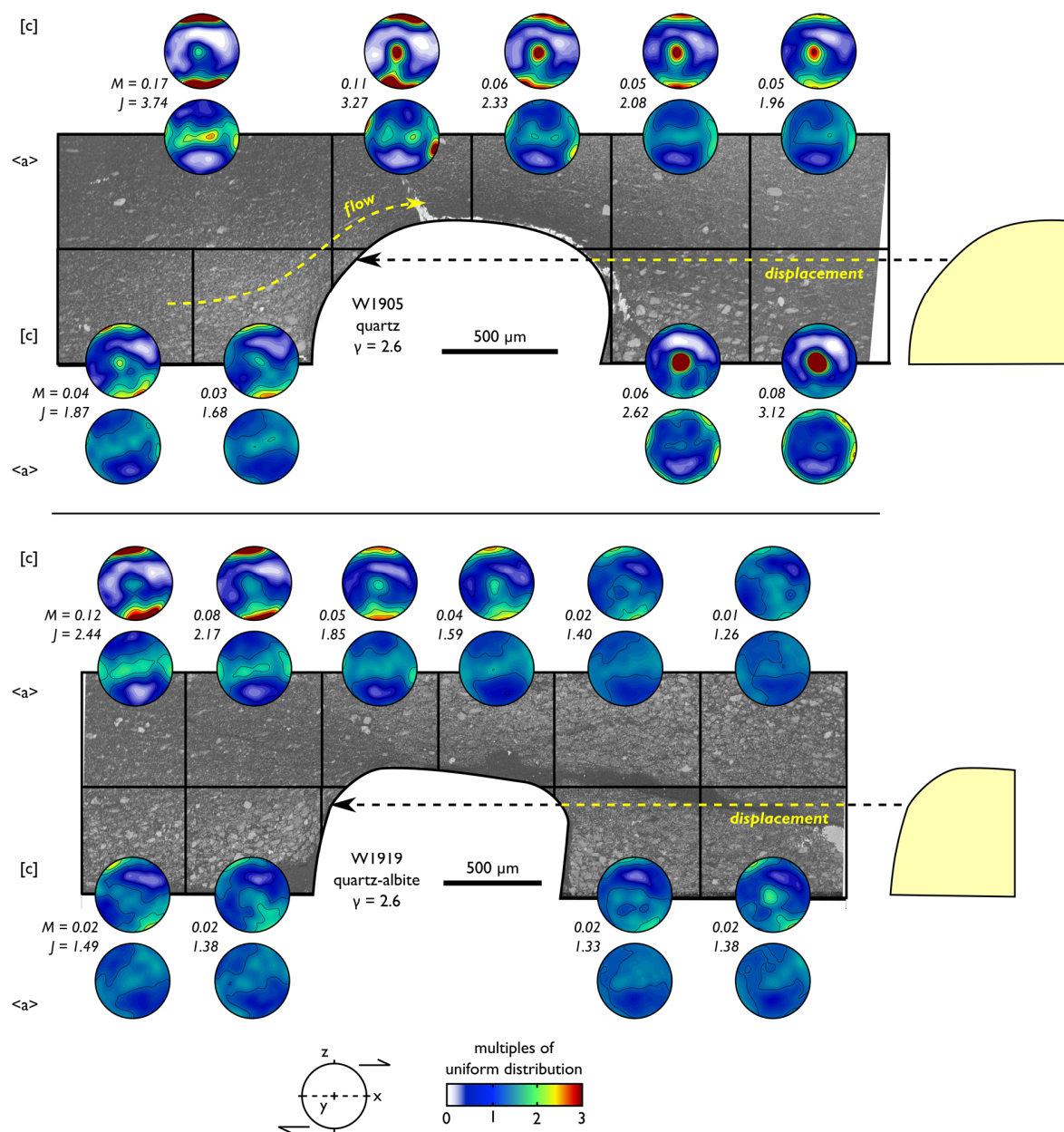


Fig. DR2: Evolution of quartz [c] and <a> axes during shear of quartz (top panel) and quartz with 25 vol.% albite (bottom panel) around a cylindrical piston asperity. Pole figures are constructed in the same manner as Fig. 3.

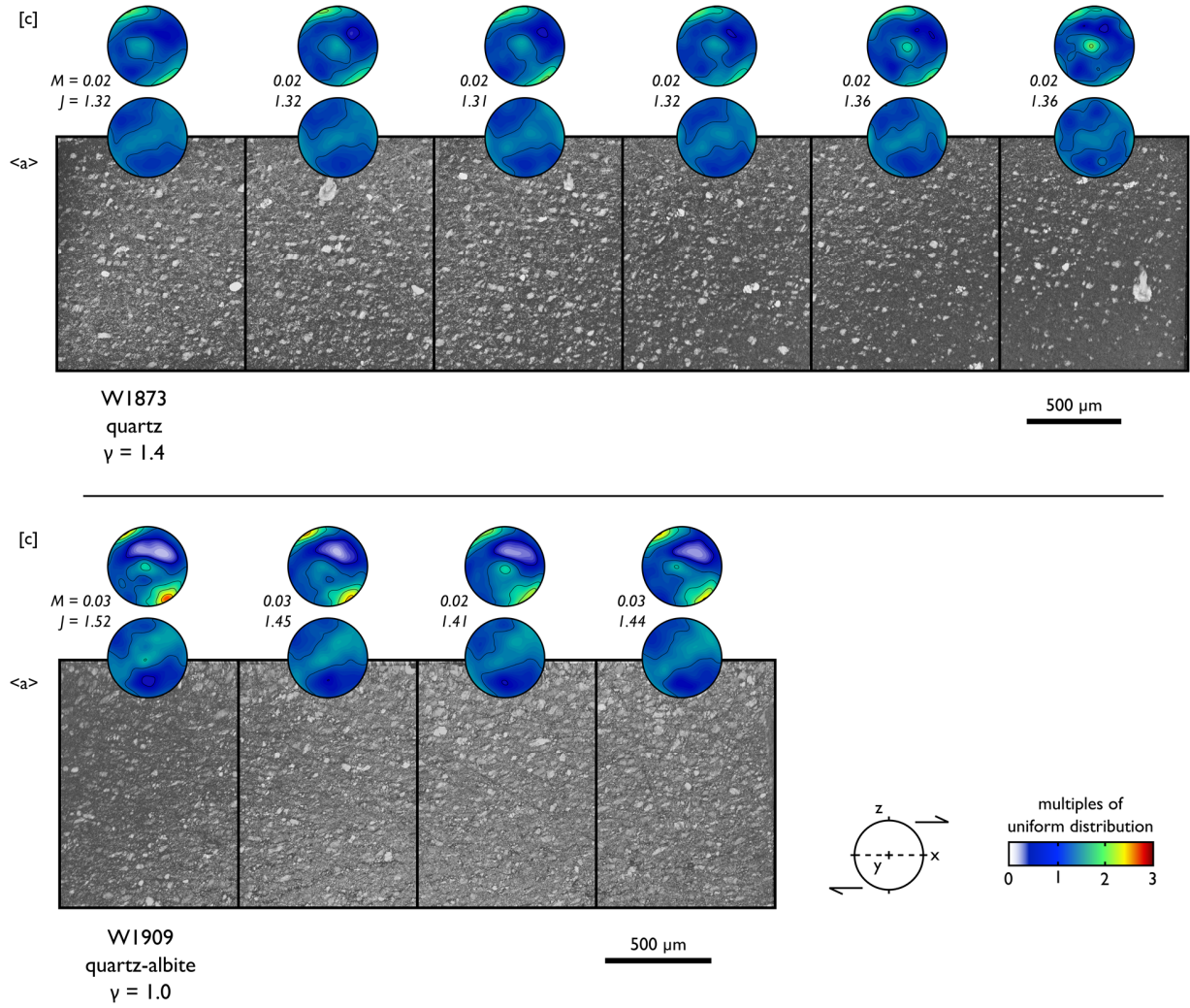


Fig. DR3: Evolution of quartz [c] and $\langle a \rangle$ axes during shear of quartz (top panel) and quartz with 25 vol.% albite (bottom panel) using planar pistons. Pole figures are constructed in the same manner as Fig. 3. Note that shear strains (and therefore CPO intensities) in these experiments are lower than those in the asperity experiments. However, similar CPOs can be seen: y_{\max} dominated [c]-axes in the quartz experiments, z_{\max} dominated [c]-axes in the quartz-albite experiments.

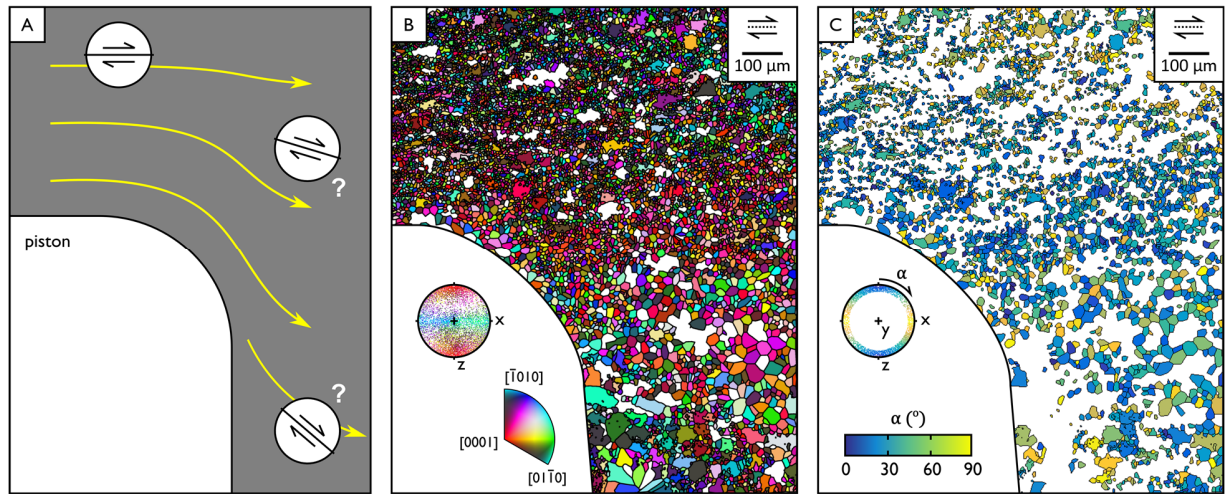


Fig. DR4: A) Material flow paths are modified around piston asperity corners, and may be responsible for CPO rotation. B) Map of quartz grains (quartz-albite sample W1921), colored by their orientation with respect to the pole to shear plane (z-direction). C) quartz grains within 20° of the x-z plane, colored by the angle, α , between their [c]-axis and the z-direction. There is no clear systematic rotation of [c]-axis during shear around the piston asperity corner.